AAS 22-174

VELOCIMETER LIDAR-BASED RELATIVE RATE ESTIMATION FOR AUTONOMOUS RENDEZVOUS, PROXIMITY OPERATIONS, AND DOCKING APPLICATIONS

Davis Adams[*], **Manoranjan Majji**[†]
Texas A&M University, College Station, TX, 77843-3141

This paper presents a navigation system for autonomous rendezvous, proximity operations, and docking (RPOD) with respect to non-cooperative space objects using a novel velocimeter light detection and ranging (LIDAR) sensor. Given only raw position and Doppler velocity measurements, the proposed methodology is capable of estimating the six degree-of-freedom (DOF) relative velocity without any *a priori* information regarding the body of interest. Further, the raw Doppler velocity measurement field directly exposes the body of interest's center of rotation (i.e. center of mass) enabling precise 6-DOF pose estimation if the rate estimates are fused within a Kalman filter architecture. These innovative techniques are computationally inexpensive and do not require information from peripheral sensors (i.e. gyroscope, magnetometer, accelerometer etc.). The efficacy of the proposed algorithms were evaluated via emulation robotics experiments at the Land, Air and Space Robotics (LASR) laboratory at Texas A&M University. Although testing was completed with a single body of interest, this approach can be used to online estimate the 6-DOF relative velocity of any amount of non-cooperative bodies within the field-of-view.

INTRODUCTION

The field of autonomous rendezvous, proximity operations, and docking (RPOD) encompasses a wide array of increasingly important relative spacecraft applications such as active debris removal (ADR), satellite servicing and assembly, asteroid sampling, and formation flying. These missions require technologies suitable for both cooperative and non-cooperative bodies of interest, thus, one particularly challenging aspect of RPOD applications is the development and implementation of autonomous on-board systems capable of sensing and reacting to highly uncertain dynamic conditions in a reliable manner. Further, according to Naasz and Moreau [1], mainstream RPOD technology for wide spectrums of missions does not currently exist causing new missions requiring autonomous RPOD capabilities to incur significant non-recurring engineering and development costs related to sensors and integrated systems. Although the use of inertial sensors, such as gyroscopes and accelerometers, have become ubiquitous in spacecraft navigation, these sensors cannot deliver any useful information regarding the relative motion between two or more bodies. In the context of non-cooperative proximity operations, this leads to the need for additional sensing mechanisms.

The key challenge in carrying out proximity operations with non-cooperative space objects is the notion that the 6-DOF relative rates (translational and angular velocity) are highly uncertain and

[*]Graduate Research Assistant, Land, Air and Space Robotics (LASR) Laboratory, Aerospace Engineering
[†]Assistant Professor, Director, Land, Air and Space Robotics (LASR) Laboratory, Aerospace Engineering

directly influence the precision of any position estimates. Consistently successful RPOD missions require a high-degree of confidence for both the relative pose and rate estimates as any guidance and control action in the presence of large uncertainty can prove fatal. In order to ascertain estimates with the required precision and confidence, the spacecraft engaging in proximity operations typically has to expend a lot of time and computational resources due to complex computer vision data processing algorithms and the implementation of a navigation filter. In previous research, many solutions have been developed to sense the relative motion states. The Land, Air, and Space Robotics (LASR) laboratory at Texas A&M has made significant contributions with regards to various sensing technologies including stereo-vision and light detection and ranging (LIDAR) systems for close proximity spacecraft navigation [2, 3, 4, 5, 6, 7].

Innovations in the autonomous automotive industry offer an exciting new basis for the sensing of relative motion between two or more tumbling rigid bodies. The LASR laboratory has recently acquired one such revolutionary LIDAR sensor system which can simultaneously acquire a dense point cloud (3D points associated with objects within the field-of-view), point-wise Doppler velocity measurements, a co-registered image stream and an infra-red (IR) response of the environment from the sensor point of view. This paper aims to leverage this wealth of knowledge to produce an innovative 6-DOF relative velocity estimator without the need for additional peripheral sensors or a predefined object model. Emulation robotics experiments are performed to demonstrate the efficacy of the proposed algorithms in a real-time RPOD scenario such as soft-capture of a rocket body as displayed in Fig. 1.

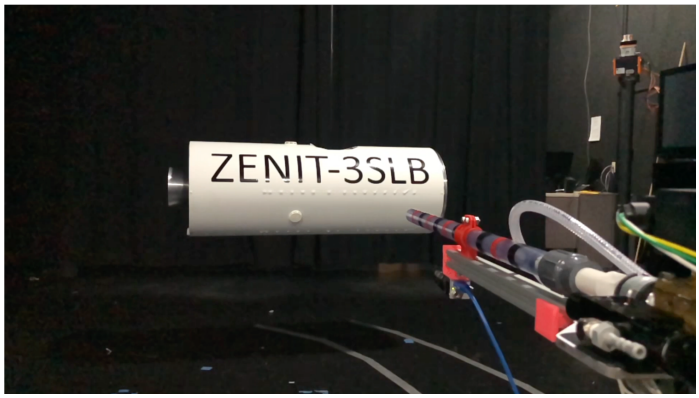

Figure 1. Proximity Operation Emulation Robotics at Land, Air and Space Robotics Laboratory

The rest of the paper is organized as follows. Section II derives the velocimeter LIDAR based spacecraft relative navigation problem from first principles. Next, Section III presents a novel batch state estimation algorithm that can directly estimate the relative 6-DOF translational and rotational velocities of a body of interest (BOI) using linear system theory. Section IV delivers the experimental methodology and results of employing the proposed techniques to estimate the relative velocities of a rotating rocket body. Finally, Section V summarizes the mathematical formulations, navigation methodologies, and experimental results and provides conclusions drawn from the work.

VELOCIMETER LIDAR RELATIVE NAVIGATION

LIDAR sensing units offer an advantageous means to determining the relative 6-DOF pose and velocity of a non-cooperative body during RPOD missions. In contrast to 3D LIDAR-based ap-

proaches, standard photogrammetry methods [8] acquire and track 2D features over a sequence of frames to obtain relative pose estimates. These methods exhibit many drawbacks including significant sensitivity to lighting conditions, added difficulty during multi-body segmentation, and the reliance on pre-calibrated camera parameters and pre-defined camera models to infer depth. Alternatively, LIDAR units provide direct depth information and are not affected by variable lighting conditions. Moreover, a state-of-the-art velocimeter LIDAR capable of measuring point-wise relative Doppler velocity, which is defined as the projection of the 6-DOF relative velocity onto the line-of-sight vector, can further refine pose estimates. A mathematical description of relative navigation using a velocimeter LIDAR is given below.

Consider a chaser spacecraft with known position, orientation, and motion observing a non-cooperative body-of-interest (BOI) within as displayed in Fig. 2. The position of an arbitrary point on the uncooperative body (${}^{B}\mathbf{p}_i$) coordinatized in the LIDAR reference frame is given by

$$ {}^{L}\mathbf{p}_{k_i} = C_{L/B_k}\,{}^{B}\mathbf{p}_i + {}^{L}\mathbf{t}_k \tag{1} $$

where the left superscripts denote the frame in which a vector is coordinatized, the right subscript, k, denotes the current time-step, the right sub-subscript, $i = 1, \ldots, N_k$, denotes the i^{th} point on the body, C_{L/B_k} is the direction cosine matrix mapping vectors in the current body frame, B, to the LIDAR frame, L, and ${}^{L}\mathbf{t}_k$ is the relative translation vector between the origin of the LIDAR frame to body's center-of-mass.

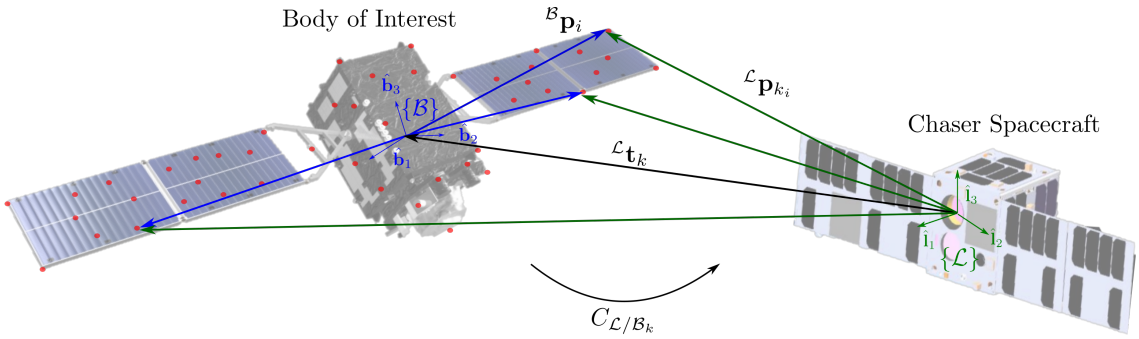

Figure 2. Relative position between the LIDAR reference frame on chaser spacecraft and an arbitrary point on a body of interest

Taking the time derivative of Eqn. (1) leads to the relative velocity of the i^{th} point on the body resulting in

$$ {}^{L}\mathbf{v}_{k_i} = -\left[{}^{L}\boldsymbol{\omega}_k{}^{\times}\right] C_{L/B_k}\,{}^{B}\mathbf{p}_i + {}^{L}\dot{\mathbf{t}}_k + C_{L/B_k}\,{}^{B}\dot{\mathbf{p}}_i \tag{2} $$

where $[\cdot^{\times}]$ denotes the skew symmetric cross product matrix of a vector, ${}^{L}\dot{\mathbf{t}}_k$ is the relative translational velocity of the non-cooperative body, and ${}^{L}\boldsymbol{\omega}_k$ is the relative angular velocity from the body frame to the LIDAR frame. This work only considers situations where the non-cooperative body is rigid; therefore, ${}^{B}\dot{\mathbf{p}}_i = 0 \;\forall\; i$. Furthermore, Eqn. (2) can be rewritten to be linear in ${}^{L}\boldsymbol{\omega}_k$ by reversing the cross product resulting in

$$ {}^{L}\mathbf{v}_{k_i} = \left[(C_{L/B_k}\,{}^{B}\mathbf{p}_i)^{\times}\right] {}^{L}\boldsymbol{\omega}_k + {}^{L}\dot{\mathbf{t}}_k \tag{3} $$

Now consider the line-of-sight (LOS) velocity (or Doppler velocity) of the i^{th} point on the body from the LIDAR's perspective to be

$$\begin{aligned} \tilde{v}_{k_i} &= \frac{{}^{L}\mathbf{p}_{k_i}{}^{T}\,{}^{L}\mathbf{v}_{k_i}}{\|{}^{L}\mathbf{p}_{k_i}\|} \\ &= \frac{1}{\|{}^{L}\mathbf{p}_{k_i}\|}({}^{L}\mathbf{p}_{k_i}{}^{T}\left[(C_{L/B_k}\,{}^{B}\mathbf{p}_i)^{\times}\right]{}^{L}\boldsymbol{\omega}_k + {}^{L}\mathbf{p}_{k_i}{}^{T}\,{}^{L}\dot{\mathbf{t}}_k) \end{aligned} \tag{4}$$

where $\|\cdot\|$ is the magnitude of the corresponding vector. It is important to note that Eqn. (4) is linear in both angular and translational velocity. A representative display of the raw measured LOS velocity versus the expected LOS velocity given the true angular velocity is shown in Fig. 3. Notice that the expected velocity distribution has higher positive velocity values on the right side of the body than the measured. This can be attributed to an incorrect center-of-mass (COM) estimate which was placed at the point cloud centroid to produce the estimated Doppler velocity distribution presented in Fig. 3.

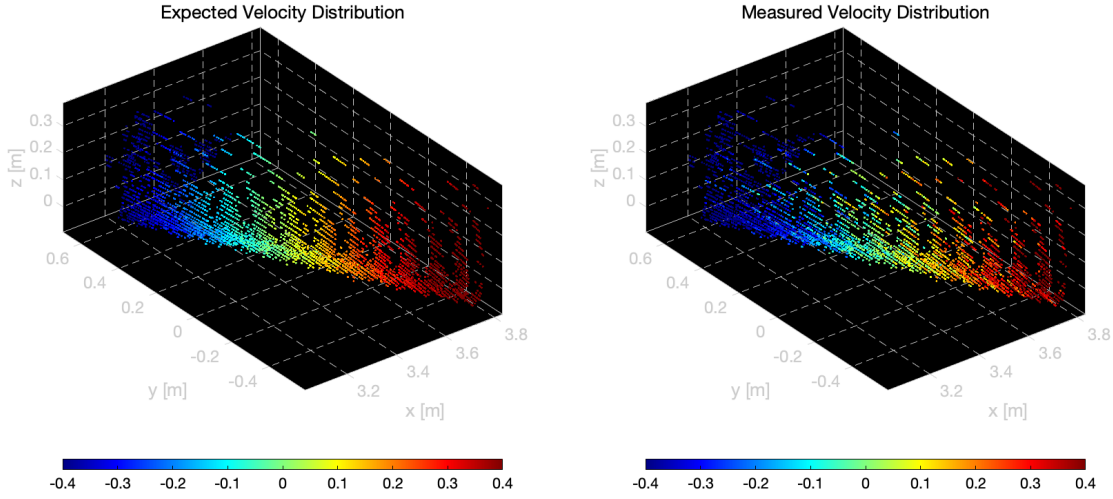

Figure 3. Expected LOS velocity distribution (left) vs. measured (right)

The inability to accurately determine a non-cooperative body's center-of-mass is one of the main sources of error when it comes to relative rate estimation for RPOD applications. Interestingly, the Doppler velocity field directly exposes the true center of rotation (i.e. center of mass) of the BOI. Briefly consider the velocity measurement field to be a function of one positional coordinate at a time. Fig. 4 displays these three independent functions of space. It is natural to suggest that the body's center of mass lies where the velocity field as a function of position changes sign. In other words, the values of where the three functions displayed in Fig. 4 cross zero ($\tilde{v}_{k_i} = 0$) are the respective (x,y,z) coordinates of the COM for that particular configuration. Assuming the current direction cosine matrix which maps the body frame to the LIDAR frame is known, this direct knowledge of the COM allows the collection of points which make up the BOI coordinatized in the body frame, ${}^{B}\mathbf{p}_i$, to be extracted.

For each frame, position and LOS velocity measurements are acquired from the velocimeter LIDAR (i.e. ${}^{L}\mathbf{p}_{k_i}$ and $\tilde{v}_{k_i}$ respectively) for every point within the FOV. Given this information, the next step is to segment out independent bodies (if more than one are visible) and determine

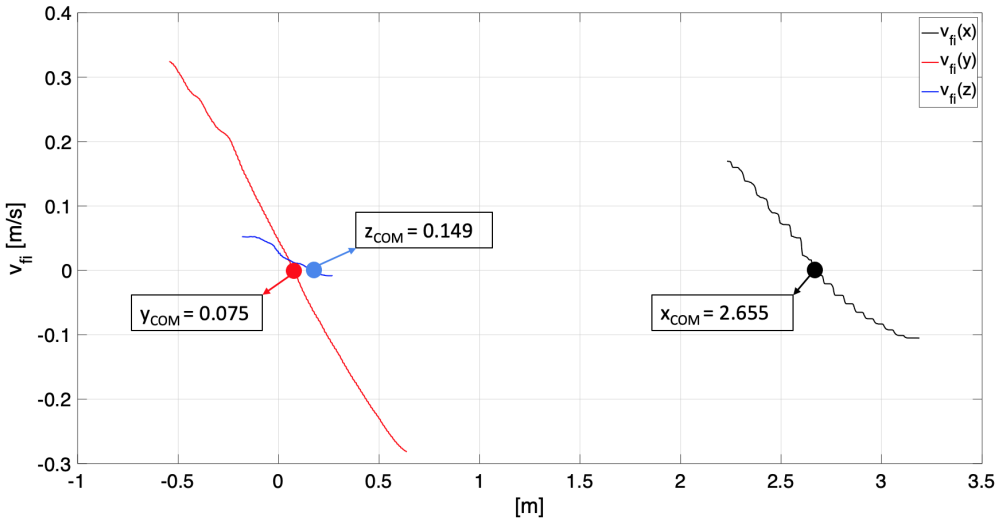

Figure 4. Doppler velocity field as an independent function of (x,y,z) exposing the true center-of-mass

each body's relative position and orientation. Significant research has been done to address these issues including point cloud registration techniques, 3D point feature matching, and various types of navigation filters [9, 10, 11, 12, 13, 14, 15, 16, 17, 18]. This work implements cluster segmentation to separate the various independent bodies within the FOV, and an iterative closest point (ICP) algorithm to determine the frame-to-frame relative change in orientation and position of the body of interest.

BATCH STATE ESTIMATION

Assuming the frame-to-frame relative orientation and translation (C_{L/B_k} and ${}^{L}\mathbf{t}_k$, respectively) between the non-cooperative body and the LIDAR can successfully be extracted through point cloud registration techniques, the main issue of estimating the body's relative angular and translational velocity can now be addressed. If embedded into a Kalman filter framework, direct velocity information would help refine the position estimate, and, most notably, aid in the determination and tracking of the true center of mass. It is important to note that existing point cloud registration techniques assume that the segmented point cloud centroid is the body's center of mass. This is not the case for the majority of real world applications, especially when the BOI is not fully captured in the point cloud. Therefore, any angular velocity estimates derived from this information is sure to be inaccurate. Further, up until the introduction of Doppler velocimeter measurement units, bulk velocity could only be inferred from position estimates, leading to error propagation. While position-informed navigation filters can mitigate and control this error, significant computational effort must be employed to provide reasonable rate estimates. To this end, a simplified approach to extract the relative translational and angular velocities by leveraging relative state kinematics and dynamics has been developed and is presented below.

As aforementioned, the LOS velocity measurement provided by the velocimeter LIDAR is linear in relative translational and angular velocity which can directly be observed by rewriting Eqn. 3 in

matrix form as

$$\tilde{v}_{k_i} = \begin{bmatrix} \frac{{}^L\mathbf{p}_{k_i}}{\|{}^L\mathbf{p}_{k_i}\|} & \frac{{}^L\mathbf{p}_{k_i}{}^T\left[(C_{L/B_k}{}^B\mathbf{p}_i)^\times\right]}{\|{}^L\mathbf{p}_{k_i}\|} \end{bmatrix} \begin{bmatrix} {}^L\dot{\mathbf{t}}_k \\ {}^L\boldsymbol{\omega}_k \end{bmatrix} \tag{5}$$

Linear system theory suggests that upon reception of each point cloud, consisting of N 3D points with corresponding Doppler velocities, an over-constrained set of linear equations of the form $\mathbf{y} = H\mathbf{x}$ where $\mathbf{y} \in R^{N\times 1}$, $H \in R^{N\times 6}$, and $\mathbf{x} \in R^{6\times 1}$ can be constructed to instantaneously solve for translational and angular velocity via least squares techniques. However, initial tests revealed the ill-conditioned nature of the H matrix which led to erroneous estimates of the velocity states with extremely large error covariance. The condition number of the system, κ, defined by the ratio of the largest to the smallest singular value of H^TH, was on the order of $\kappa \sim \mathcal{O}(1e7)$.

To surmount this issue, regularization techniques can be implemented to aid in the conditioning of the system, as performed by Hu et al. [19]. However, selection of regularization values is an arbitrary process and this work found it to produce erroneous results due to a single viewpoint in contrast to Hu's multi-view setup. Another approach to aid in conditioning is to augment the original system with other linear systems that are functions of the same independent variables. With this in mind, consider the Doppler velocity measurement field to be a continuous function of space and time, i.e. $\tilde{v}_{k_i} = \tilde{v}_{k_i}(t, \mathcal{X})$, where $\mathcal{X}$ defines an inertial Cartesian coordinate system with (x,y,z) components. Assuming that over a period of time, the BOI is not accelerating in any direction, the Lagrangian (or material) derivative of the Doppler velocity field can be set to 0 as

$$\frac{D\tilde{v}_{k_i}}{Dt} = \frac{\partial \tilde{v}_{k_i}}{\partial t} + \mathbf{v}_{fi} \cdot \nabla \tilde{v}_{k_i} = 0 \tag{6}$$

where ∇ is the gradient operator and $\mathbf{v}$ is given by Eqn. (3). Ignoring higher order terms from the partial derivative term, Eqn. (6) can be rewritten in matrix form to be

$$\begin{aligned} \frac{D\tilde{v}_{k_i}}{Dt} = 0 &= \mathbf{v}^T \nabla \tilde{v}_{k_i} \\ &= \begin{bmatrix} \frac{\partial \tilde{v}_{k_i}}{\partial x} & \frac{\partial \tilde{v}_{k_i}}{\partial y} & \frac{\partial \tilde{v}_{k_i}}{\partial z} \end{bmatrix} \mathbf{v} \\ &= \begin{bmatrix} \frac{\partial \tilde{v}_{k_i}}{\partial x} & \frac{\partial \tilde{v}_{k_i}}{\partial y} & \frac{\partial \tilde{v}_{k_i}}{\partial z} \end{bmatrix} \begin{bmatrix} I_{3\times 3} & \left[(C_{L/B_k}{}^B\mathbf{p}_i)^\times\right] \end{bmatrix} \begin{bmatrix} {}^L\dot{\mathbf{t}}_k \\ {}^L\boldsymbol{\omega}_k \end{bmatrix} \end{aligned} \tag{7}$$

where the values in the matrix $\begin{bmatrix} \frac{\partial \tilde{v}_{k_i}}{\partial x} & \frac{\partial \tilde{v}_{k_i}}{\partial y} & \frac{\partial \tilde{v}_{k_i}}{\partial z} \end{bmatrix}$ can be numerically approximated from measurement data for each frame. The system presented by Eqn. (7) alone was not enough to improve the condition of the original system to the point where accurate estimates could be obtained. Therefore, attitude kinematics can be leveraged to produce another linear system as a function of the body's angular velocity to further refine the conditioning of the total system. Employing Classical Rodrigues Parameters (CRPs) to parameterize the body's orientation with respect to the LIDAR frame, the following linear system is obtained [20]:

$$\dot{\boldsymbol{\beta}}_f = \begin{bmatrix} \dot{\beta}_{1_f} \\ \dot{\beta}_{2_f} \\ \dot{\beta}_{3_f} \end{bmatrix} = \begin{bmatrix} 0_{3\times 3} & \frac{1}{2}\left[I_{3\times 3} + \left[\boldsymbol{\beta}_f^\times\right] + \boldsymbol{\beta}_f\boldsymbol{\beta}_f^T\right] \end{bmatrix} \begin{bmatrix} {}^L\dot{\mathbf{t}}_k \\ {}^L\boldsymbol{\omega}_k \end{bmatrix} \tag{8}$$

where the values $\begin{bmatrix} \dot{\beta}_{1_f} & \dot{\beta}_{2_f} & \dot{\beta}_{3_f} \end{bmatrix}^T$ can be numerically approximated from measurement data for each frame and the vector of CRPs, $\boldsymbol{\beta}$, can directly be extracted from C_{L/B_k} [20]. The only unknowns within the systems presented in Eqns. 7 and 8 are the velocity state vector variables so

they can directly be appended to the linear system represented in Eqn. (5). Therefore, assuming the relative angular and translational velocity remain constant over a 'batch' of F frames with N_f measurements per frame (assuming there will be a varying number of measurements per frame) the following set of linear equations can be formed as

$$\begin{bmatrix} \tilde{v}_{fi} \\ \hdashline 0 \\ \hdashline \dot{\boldsymbol{\beta}}_f \end{bmatrix} = \begin{bmatrix} \frac{\mathbf{p}_{f_i}^T}{\|\mathbf{p}_{k_i}\|} & \frac{\mathbf{p}_{f_i}^T\left[(C_{f/k-F}\mathbf{p}_{k-F_i})^\times\right]}{\|\mathbf{p}_{k_i}\|} \\ \hdashline \nabla\tilde{v}_f^T & \nabla\tilde{v}_f^T\left[(C_{f/k-F}\mathbf{p}_{k-F_i})^\times\right] \\ \hdashline 0_{3\times3} & \frac{1}{2}\left[I_{3\times3} + \left[\boldsymbol{\beta}_f^\times\right] + \boldsymbol{\beta}_f\boldsymbol{\beta}_f^T\right] \end{bmatrix} \begin{bmatrix} {}^L\dot{\mathbf{t}}_k \\ {}^L\boldsymbol{\omega}_k \end{bmatrix} \tag{9}$$

$$\begin{bmatrix} \tilde{v}_{11} \\ \vdots \\ \tilde{v}_{1N_1} \\ \vdots \\ \tilde{v}_{F1} \\ \vdots \\ \tilde{v}_{FN_F} \\ \hdashline 0 \\ \vdots \\ 0 \\ \vdots \\ 0 \\ \vdots \\ 0 \\ \hdashline \dot{\beta}_{1_1} \\ \dot{\beta}_{2_1} \\ \dot{\beta}_{3_1} \\ \vdots \\ \dot{\beta}_{1_F} \\ \dot{\beta}_{2_F} \\ \dot{\beta}_{3_F} \end{bmatrix} = \begin{bmatrix} \frac{{}^L\mathbf{p}_{11}{}^T}{\|{}^L\mathbf{p}_{11}\|} & \frac{{}^L\mathbf{p}_{11}{}^T\left[(C_{L/B_1}{}^B\mathbf{p}_1)^\times\right]}{\|{}^L\mathbf{p}_{11}\|} \\ \vdots & \vdots \\ \frac{{}^L\mathbf{p}_{1N_1}{}^T}{\|{}^L\mathbf{p}_{1N_1}\|} & \frac{{}^L\mathbf{p}_{1N_1}{}^T\left[(C_{L/B_1}{}^B\mathbf{p}_{N_1})^\times\right]}{} \\ \vdots & \vdots \\ \frac{{}^L\mathbf{p}_{F1}{}^T}{\|{}^L\mathbf{p}_{F1}\|} & \frac{{}^L\mathbf{p}_{F1}{}^T\left[(C_{L/B_F}{}^B\mathbf{p}_1)^\times\right]}{\|{}^L\mathbf{p}_{F1}\|} \\ \vdots & \vdots \\ \frac{{}^L\mathbf{p}_{FN_F}{}^T}{\|{}^L\mathbf{p}_{FN_F}\|} & \frac{{}^L\mathbf{p}_{FN_F}{}^T\left[(C_{L/B_F}{}^B\mathbf{p}_{N_F})^\times\right]}{\|{}^L\mathbf{p}_{FN_F}\|} \\ \hdashline \nabla\tilde{v}_{11}^T & \nabla\tilde{v}_{11}^T\left[(C_{L/B_1}{}^B\mathbf{p}_1)^\times\right] \\ \vdots & \vdots \\ \nabla\tilde{v}_{1N_1}^T & \nabla\tilde{v}_{1N_1}^T\left[(C_{L/B_1}{}^B\mathbf{p}_{N_1})^\times\right] \\ \vdots & \vdots \\ \nabla\tilde{v}_{F1}^T & \nabla\tilde{v}_{F1}^T\left[(C_{L/B_F}{}^B\mathbf{p}_1)^\times\right] \\ \vdots & \vdots \\ \nabla\tilde{v}_{FN_F}^T & \nabla\tilde{v}_{FN_F}^T\left[(C_{L/B_F}{}^B\mathbf{p}_{N_F})^\times\right] \\ \hdashline 0_{3\times3} & \frac{1}{2}\left[I_{3\times3} + \left[\boldsymbol{\beta}_1^\times\right] + \boldsymbol{\beta}_1\boldsymbol{\beta}_1^T\right] \\ \vdots & \vdots \\ 0_{3\times3} & \frac{1}{2}\left[I_{3\times3} + \left[\boldsymbol{\beta}_F^\times\right] + \boldsymbol{\beta}_F\boldsymbol{\beta}_F^T\right] \end{bmatrix} \begin{bmatrix} {}^L\dot{\mathbf{t}}_k \\ {}^L\boldsymbol{\omega}_k \end{bmatrix} \tag{10}$$

for $f = k-F+1,\ldots,k$ and $i = 1,\ldots,N_f$ where $\nabla\tilde{v}_{k_i}^T = \begin{bmatrix} \frac{\partial\tilde{v}_{k_i}}{\partial x} & \frac{\partial\tilde{v}_{k_i}}{\partial y} & \frac{\partial\tilde{v}_{k_i}}{\partial z} \end{bmatrix}$ and $C_{f/k-F}$ is the direction cosine matrix mapping the BOI's $(k-F)$ frame to the LIDAR's f frame.

Analysis of this new system indicated a significant improvement in the condition number such that, $\kappa \sim \mathcal{O}(1e3)$, and is also much more capable of estimating bulk velocities with higher confidence as indicated by the resultant error covariance, which is defined below. Although implementing a standard least squares estimator for each batch of frames can provide decent velocity estimates, employing this framework in a sequential manner can significantly refine the results. This sequential batch least squares framework is detailed in [21], however for completeness, the key steps are detailed below.

First, consider every F frames to be defined as a 'batch'. If the total number of points acquired over the current batch of F frames is defined to be $N_T = \sum_f^k N_f$, consider the linear system presented by Eqn. (10) to take the form $\mathbf{y}_1 = H_1\mathbf{x}_1$ where $\mathbf{y}_1 \epsilon R^{(2N_T+3F)\times 1}$, $H_1 \epsilon R^{(2N_T+3F)\times 6}$, and $\mathbf{x}_1 \epsilon R^{6\times 1}$. Now consider the measurement equation to be $\tilde{\mathbf{y}}_1 = H_1\mathbf{x}_1 + \mathbf{n}_1$ where $\mathbf{n}$ is a vector of measurement errors. It is important to note that the Doppler velocity measurements are the only terms with a true associated uncertainty; however, to avoid numerical instability, a very small error term is added to the linear systems given in Eqns. (7) and (8). Thus, once the first 'batch' of data is acquired, the instantaneous velocity vector can be solved for by employing a linear least squares framework yielding

$$\hat{\mathbf{x}}_1 = (H_1^T W_1 H_1)^{-1} H_1^T W_1 \tilde{\mathbf{y}}_1 \tag{11}$$

where the $[\hat{\cdot}]$ notation denotes an estimated quantity and W is a positive definite weighting matrix. The weighting matrix is said to be 'optimal' if it is set to the inverse of the observation error covariance defined as $E\{\mathbf{n}\mathbf{n}^T\}^{-1}$ where $E\{\cdot\}$ is the expectation operator. However, it was found that simply setting the weighting matrix to an appropriately sized Identify matrix produces accurate and precise results. The estimation error covariance for the first estimate is defined by $P_1 = E\{\boldsymbol{\delta}\mathbf{x}_1\boldsymbol{\delta}\mathbf{x}_1^T\} = \left[H_1^T W_1 H_1\right]^{-1}$ where $\boldsymbol{\delta}\mathbf{x}$ is the estimation error. The first estimate acts as a baseline that is subsequently updated with each new batch of data contained in $\tilde{\mathbf{y}}_2$ and H_2. This corrections are performed as follows [22]:

$$\hat{\mathbf{x}}_2 = \left[H_1^T W_1 H_1 + H_2^T W_2 H_2\right]^{-1} \left(H_1^T W_1 \tilde{\mathbf{y}}_1 + H_2^T W_2 \tilde{\mathbf{y}}_2\right) \tag{12}$$

$$P_2 = \left[H_1^T W_1 H_1 + H_2^T W_2 H_2\right]^{-1} \tag{13}$$

It is natural to see the relationship between these two expressions is given by

$$P_2^{-1} = P_1^{-1} + H_2^T W_2 H_2 \tag{14}$$

To avoid the inversion of the covariance matrix at every time step, which could lead to numerical instability, the following covariance recursion form of the sequential linear least squares algorithm can be employed:

$$\hat{\mathbf{x}}_{k+1} = \hat{\mathbf{x}}_k + K_{k+1}(\tilde{\mathbf{y}}_{k+1} - H_{k+1}\hat{\mathbf{x}}_k) \tag{15}$$

where

$$K_{k+1} = P_k H_{k+1}^T \left[H_{k+1} P_k H_{k+1}^T + W_{k+1}^{-1}\right]^{-1} \tag{16}$$

$$P_{k+1} = \left[I - K_{k+1} H_{k+1}\right] P_k \tag{17}$$

It is important to note that Joseph's stability update form can be, and was, used in this sequential linear estimator framework. Recall the weighting matrix, W_{k+1}, was set to identity for this application: a non-optimal selection. According to Zanetti and DeMars [23], Joseph's stability update form alleviates any numerical instability or improper over-corrections due to the use of a non-optimal weighting matrix.

Both the standard and sequential batch state estimation methodologies can be implemented in one of two ways. First, after each 'batch' of F frames are received, the set of linear equations given by Eqn. (10) can be constructed and an estimation can be obtained using the update equations. However, this limits the estimation frequency to F times the data reception rate. Early tests indicated that at least 2 frames of data are needed to obtain accurate estimates for the translational and angular velocity. It was found that the error covariance decreased as the number of frames included in each

batch increased. Therefore, there is a dichotomy between faster updates and confident estimates that must be judiciously balanced according to the mission requirements. The second method of implementation enables estimates to be obtained at the rate of data capture by using a 'sliding window' approach. After each new frame of data is received, the measurement vector, $\tilde{\mathbf{y}}$, and linear system matrix, H, are back-filled with the last $F-1$ frames of information, and the new frame completes the 'batch'. Although this back-fill maneuver seems simple, the H matrix is comprised of direction cosine matrices which are defined with respect to the 1st frame of the current batch. Thus, the entire H matrix needs to be re-computed every frame rather than just appending the most recent frame's expressions. Although the second method is more cumbersome than the first, it allows for any number of frames per batch to be used while also enabling updates to be performed at the rate of data reception. Furthermore, it was found that using the 'sliding window' approach yields more uniform estimates in contrast to estimates that are very noisy produced by the standard batch estimation process.

EXPERIMENTAL METHODOLOGY AND RESULTS

To test the efficacy of the proposed standard and sequential batch least squares algorithms for the estimation of translational and angular velocity of a non-cooperative body, several experimental tests were performed at Texas A&M's LASR Laboratory. The experimental setup used for all emulation experiments is displayed in Fig. 5. Pictured on the left is one of LASR Lab's novel robotic platforms called Holonomic Omni-directional Motion Emulation Robot (HOMER) which is capable of unrestricted motion in all planar directions (x, y, ψ where ψ is the yaw axis) given an arbitrary trajectory. Mounted on top of HOMER is a Stewart platform which is capable of precise 6-DOF control, and mounted on top of the Stewart platform is the novel velocimeter LIDAR. The LIDAR acquires point cloud and image data at 10 Hz and exhibits a point-wise position and Doppler velocity 1σ standard deviations of 0.05 m and 0.1 m/s, respectively. An Intel NUC was used as the compute element. Displayed in the right is LASR Lab's Suspended Target Emulation Pendulum (STEP) with a mock rocket body mounted to the end of the pendulum. STEP is a large gantry suspended above the test area and is capable of manipulating payloads in all planar directions. The LASR Lab is outfitted with Vicon motion capture system to provide ground truth data for comparison.

To ensure the proposed methodologies are capable of accurately estimating both translational and angular velocity in various conditions, two emulation experiments were implemented: 1) rocket body in a flat spin with no translation and 2) an approaching rocket body in a near pure spin. Note that the number of frames per batch was chosen to be 3 for every test case. Further, the weighting matrix for the standard batch least squares algorithm was set to identity, i.e. $W = \mathbb{I}_{N_T}$. The initial weighting matrix for the sequential batch least squares algorithm was set to $W_0 = 5 * \mathbb{I}_{N_T}$. After the first batch of data is processed and an initial estimate was obtained, the weighting matrix was set to identity.

Stationary Observation Rocket Body in a Flat Spin

The first test case emulates a (relatively) stationary chaser spacecraft in close proximity to a rocket body in a flat spin. To accomplish this, STEP was commanded to rotate the rocket body at the desired constant angular velocity of 0.25 rad/s in the yaw direction and maintain zero translational velocity in all directions. The translational and angular velocity profiles of the relative motion between the rocket body and velocimeter LIDAR coordinatized in the LIDAR reference frame is

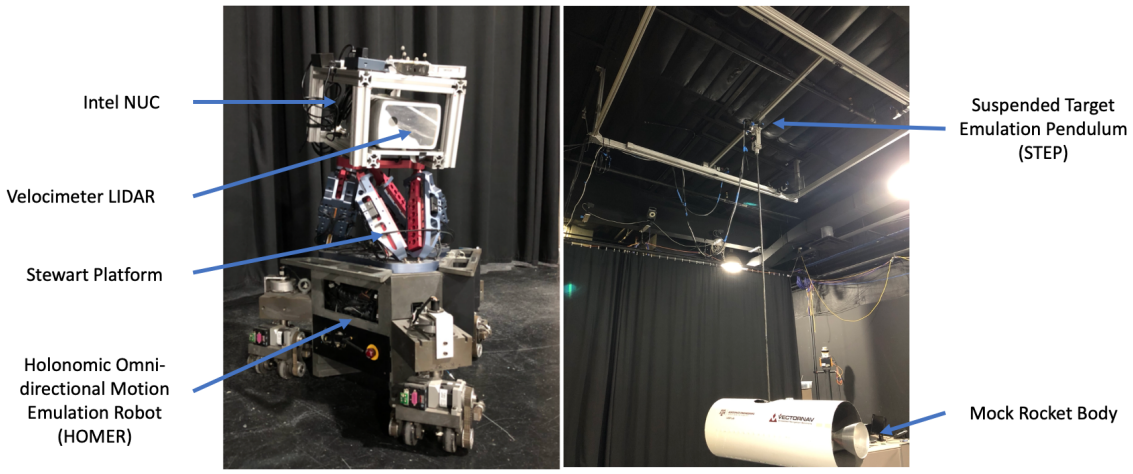

Figure 5. Experimental setup for RPOD emulation experiments at Texas A&M's Land, Air, and Space Robotics Laboratory

displayed in Fig. 6. Note that STEP has internal controllers to compensate for varying payload inertial distributions to ensure a constant angular rate. The state error and respective 3σ bound plots from the proposed regular and sequential batch least squares algorithms are displayed in Fig. 7.

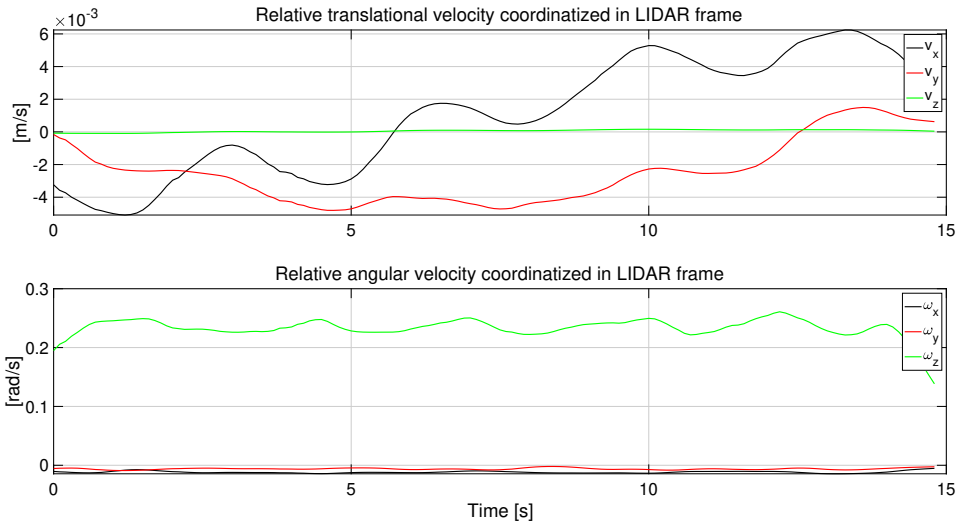

Figure 6. Translational (top) and angular (bottom) velocity profiles for a rocket body in a flat spin at 0.25 rad/s

For both the standard and sequential versions, the estimation error and error covariance is the lowest for translational velocity in the x-direction, which is expected as this is bore-sight for the velocimeter LIDAR. According to [24], the eigenvector associated with the smallest eigenvalue of the covariance matrix indicates the direction of highest observability. In this case, the direction of highest observability points almost exclusively in the direction of v_x, with similar small components in the ω_y and ω_z directions and near zero components in the other directions. Although both versions

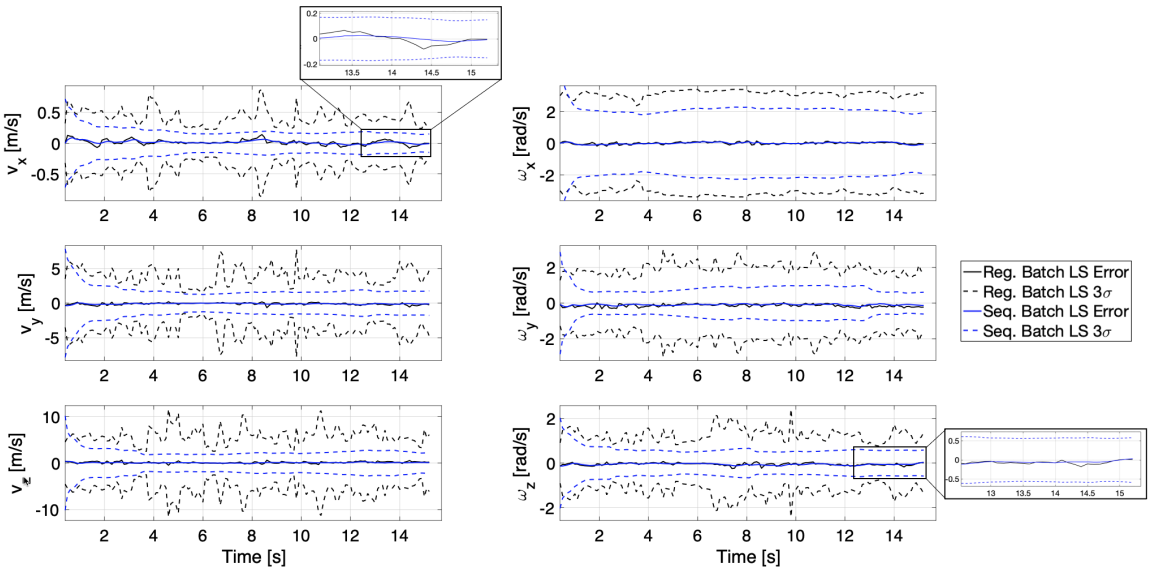

Figure 7. Translational (left) and angular (right) velocity error plots and 3σ bounds using regular and sequential linear least squares for a rocket body in a flat spin at 0.25 rad/s

of the batch least squares algorithm are able to accurately estimate the relative translational and angular motion, the sequential version can do so in a more confident and uniform manner. Most notably, the average error and 3σ standard deviation for v_x produced by the standard technique is 0.014 m/s and 0.421 m/s, respectively. Whereas the sequential variation produces an average error and converged 3σ standard deviation of 0.014 m/s and 0.145 m/s, respectively, indicating a confidence level more than 2$\times$ greater than the standard batch least squares algorithm. Moreover, the average error and 3σ standard deviation for ω_z produced by the standard technique is 0.0512 rad/s and 1.253 rad/s, respectively. Whereas the sequential version produces an average error and converged 3σ standard deviation of 0.057 rad/s and 0.580 rad/s. Despite the fact that the mean error covariance for the other velocity vector components remains large compared to the signal size, both versions of the algorithm properly estimate the zero motion as indicated by the small mean errors displayed in Table 1.

Table 1. Mean errors and 3σ standard deviations for regular and sequential batch least squares algorithms during stationary observation of a rocket body in a flat spin

	Regular Batch Least Squares		Sequential Batch Least Squares	
State	Mean Error	3σ Std. Deviation	Mean Error	Converged 3σ Std. Deviation
v_x [m/s]	0.014	0.421	0.014	0.145
v_y [m/s]	0.105	3.909	0.093	1.722
v_z [m/s]	0.116	5.819	0.079	2.171
ω_x [rad/s]	0.001	3.134	0.004	1.851
ω_y [rad/s]	0.139	1.943	0.091	0.589
ω_z [rad/s]	0.051	1.253	0.057	0.580

Approach to a Rocket Body in a Flat Spin

The second test case emulates the approach of a chaser spacecraft to a rocket body in a flat spin. To accomplish this, STEP was commanded to rotate the rocket body at the desired constant angular velocity of 0.25 rad/s in the yaw direction, translate with constant translational velocity in the x-direction and maintain zero velocity in all other directions while the LIDAR remained stationary. Note that STEP does not have control over angular motion in the x and y directions or translational motion in the z direction, so the resulting motion depicted by the velocity profiles coordinatized in the LIDAR reference frame displayed in Fig. 8 in those directions are from the natural swinging of the pendulum. This test case exhibits a much shorter test time due to space limitations. It is important to note that the proposed algorithms were derived under the assumption of constant velocity, i.e. zero acceleration. Further, the sequential version heavily relies on this assumption as it uses previous estimates to inform the current estimate. Therefore, this test case evaluates the proposed techniques' ability to maintain accuracy even when this foundational assumption is violated. The state error and respective 3σ bound plots from the proposed regular and sequential batch least squares algorithms are displayed in Fig. 9.

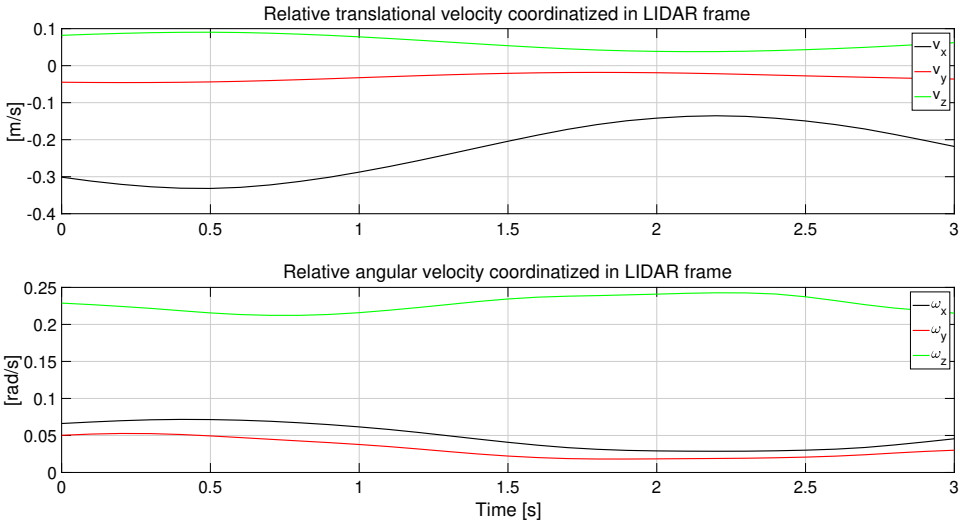

Figure 8. Translational (top) and angular (bottom) velocity profiles for an approaching rocket body in a flat spin at 0.25 rad/s

Similar to the results from the first test case, the error trajectories are completely encapsulated by their respective 3σ boundaries in all directions for both the regular and sequential batch least squares algorithms. This indicates that even under conditions when the velocity is not constant, both versions of the batch least squares algorithm can maintain consistency. Further, the notion of v_x being the most observable state is maintained as indicated by the resulting error covariance. The mean errors and 3σ standard deviations are similar to the first test case and are presented in Table 2.

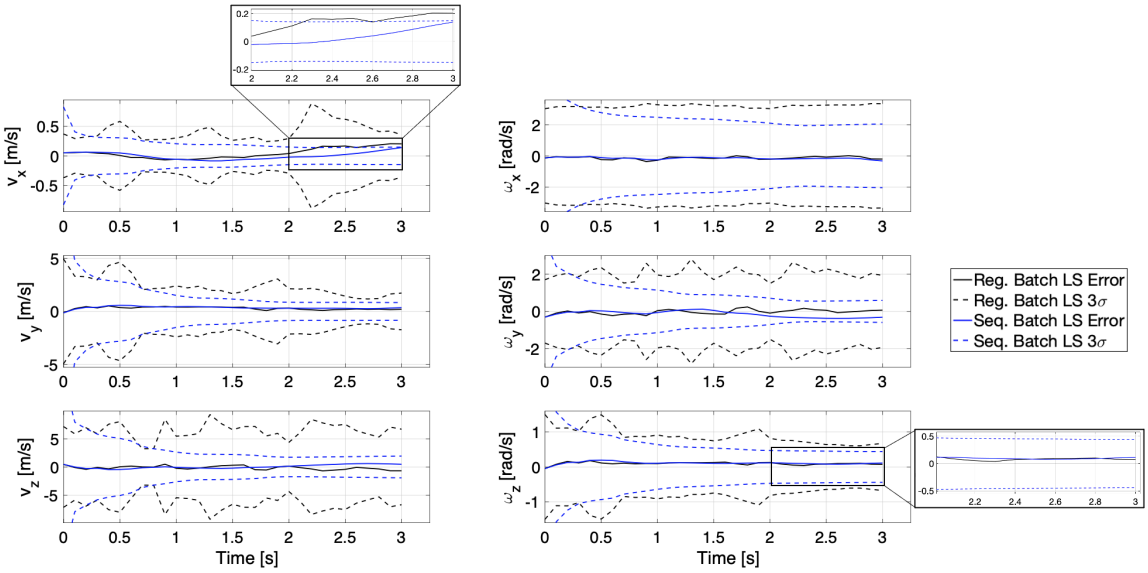

Figure 9. Translational (left) and angular (right) velocity error plots and 3σ bounds using regular and sequential linear least squares for an approaching rocket body in a flat spin at 0.25 rad/s

Table 2. Mean errors and 3σ standard deviations for regular and sequential batch least squares algorithms during approach to a rocket body in a perturbed flat spin

	Regular Batch Least Squares		Sequential Batch Least Squares	
State	Mean Error	3σ Std. Deviation	Mean Error	Converged 3σ Std. Deviation
v_x [m/s]	0.047	0.418	0.002	0.147
v_y [m/s]	0.288	2.411	0.351	0.839
v_z [m/s]	0.157	6.5074	0.064	1.935
ω_x [rad/s]	0.129	3.203	0.154	2.032
ω_y [rad/s]	0.027	2.035	0.147	0.582
ω_z [rad/s]	0.097	0.895	0.109	0.445

SUMMARY AND CONCLUSIONS

An innovative approach to simultaneously estimate the relative translational and angular velocity of an arbitrary body in the field of view of a novel velocimeter LIDAR was presented in this paper. Although testing was performed with respect to a single BOI, the proposed techniques are applicable to situations where there are multiple bodies within the FOV. Most notably, this methodology does not require any *a priori* information on the BOI or information from any other peripheral sensors to achieve accurate and confident rate estimates. Further, despite the foundational assumption of constant velocity, experimental results indicate that the proposed algorithms are capable of producing precise estimates during periods of slight acceleration. Results from the robotic emulation experiments performed at Texas A&M's Land, Air, and Space Robotics Laboratory also show that the translational velocity in the x-direction (bore-sight of the LIDAR) is the most observable velocity state. Moreover, the two representative test cases presented in this work depict the proposed methodologies' capability to accurately estimate both 6-DOF velocity in all directions. This work

is framed as a parameter estimation problem; however, future work will leverage relative motion dynamics to further refine the rate estimates as well as estimate the complete relative pose online.

ACKNOWLEDGMENTS

Partial support from National Geospatial Intelligence Agency (NGA) through Grant No. HM0476-19-1-2015 is gratefully acknowledged. Mr. Scott A. True is thanked for serving as a technical monitor. The research was carried out at Texas AM University and the Jet Propulsion Laboratory, California Institute of Technology, under a contract with the National Aeronautics and Space Administration (80NM0018D0004). Authors acknowledge JPL's SURP program to support this research. The authors also acknowledge John Carson, Ron Sostaric, Ronney Lovelace, Teming Tse, and the EG Division at NASA Johnson Space Center (JSC) for partially supporting this work through a cooperative agreement between NASA JSC and Texas AM.

REFERENCES

[1] B. J. Naasz and M. C. Moreau, "Autonomous RPOD technology challenges for the coming decade," *Advances in the Astronautical Sciences*, Vol. 144, 2012, pp. 403–425.

[2] J. L. Junkins, M. Majji, B. Macomber, J. Davis, J. Doebbler, and R. Noster, "Small Body Proximity Sensing with a Novel HD3D LADAR System," *Proceedings of the 33rd Annual AAS Guidance and Control Meeting, Breckenridge, CO; UNITED STATES;*, Advances in Astronautical Sciences, American Astronautical Society, Univelt Publications, January 2011, p. AAS 11=054.

[3] M. Majji, J. Davis, J. Doebbler, B. Macomber, J. L. Junkins, M. Vavrina, and J. Vian, "Terrain Mapping and Landing Operations using Vision Based Sensors," *Proceedings of the AIAA Guidance, Navigation and Control Conference and Exhibit*, Portland, OR, AIAA, August 2011.

[4] M. Majji and J. Junkins, "Advanced 3D sensing algorithms and computer architectures for simultaneous mapping and close proximity operations," *Proceedings of AAS Guidance, Navigation and Control Conference*, Breckenridge, CO, American Astronautical Society, February, 2012 2012.

[5] X. Wong and M. Majji, "A Structured Light System for Relative Navigation Applications," *IEEE Sensors Journal*, Vol. 16, No. 17, 2017, pp. 6662–6679.

[6] X. I. Wong and M. Majji, "Extended Kalman Filtering for Stereo Vision Based Simultaneous Location and Mapping Applications," *ASME Journal of Dynamic Systems, Measurement and Control*, Vol. 140, No. 3, 2017.

[7] C. Peck, D. W. Adams, J. McElreath, A. Verras, J. Hiemerl, M. Majji, M. Benedict, and J. Junkins, "Autonomous Deployment of Payload Packages to Spinning Rocket Bodies: Approach, Apparatus, and Emulation Using Ground Robotics," *Advances in the Astronautical Sciences*, Vol. 172, 2020.

[8] C. C. Slama, *Manual of Photogrammetry*. American Society of Photogrammetry, Falls Church, VA, 4 ed., 1980.

[9] J. L. Sell, A. Rhodes, J. O. Woods, J. A. Christian, and T. Evans, "Pose performance of LIDAR-based navigation for satellite servicing," *AIAA/AAS Astrodynamics Specialist Conference 2014*, No. August 2016, 2014, 10.2514/6.2014-4360.

[10] R. Opromolla, G. Fasano, G. Rufino, and M. Grassi, "A model-based 3D template matching technique for pose acquisition of an uncooperative space object," *Sensors (Switzerland)*, Vol. 15, No. 3, 2015, pp. 6360–6382, 10.3390/s150306360.

[11] J. O. Woods and J. A. Christian, "Lidar-based relative navigation with respect to non-cooperative objects," *Acta Astronautica*, Vol. 126, 2016, pp. 298–311, 10.1016/j.actaastro.2016.05.007.

[12] L. Liu, G. Zhao, and Y. Bo, "Point cloud based relative pose estimation of a satellite in close range," *Sensors (Switzerland)*, Vol. 16, No. 6, 2016, 10.3390/s16060824.

[13] X. Hou, C. Ma, Z. Wang, and J. Yuan, "Adaptive pose and inertial parameters estimation of free-floating tumbling space objects using dual vector quaternions," *Advances in Mechanical Engineering*, Vol. 9, No. 10, 2017, pp. 1–17, 10.1177/1687814017714210.

[14] D. Ge, D. Wang, Y. Zou, and J. Shi, "Motion and inertial parameter estimation of non-cooperative target on orbit using stereo vision," *Advances in Space Research*, Vol. 66, No. 6, 2020, pp. 1475–1484, 10.1016/j.asr.2020.05.029.

[15] X. Wang, Z. Wang, and Y. Zhang, "Stereovision-based relative states and inertia parameter estimation of noncooperative spacecraft," *Proceedings of the Institution of Mechanical Engineers, Part G: Journal of Aerospace Engineering*, Vol. 233, No. 7, 2019, pp. 2489–2502, 10.1177/0954410018782021.

[16] D. Rondao and N. Aouf, *Multi-View Monocular Pose Estimation for Spacecraft Relative Navigation*, 10.2514/6.2018-2100.

[17] Y. Feng, A. Schlichting, and C. Brenner, "3D feature point extraction from LiDAR data using a neural network," *International Archives of the Photogrammetry, Remote Sensing and Spatial Information Sciences - ISPRS Archives*, Vol. 2016-Janua, No. July, 2016, pp. 563–569, 10.5194/isprsarchives-XLI-B1-563-2016.

[18] A. Aldoma, F. Tombari, R. B. Rusu, and M. Vincze, "OUR-CVFH - Oriented, unique and repeatable clustered viewpoint feature histogram for object recognition and 6DOF pose estimation," *Lecture Notes in Computer Science*, Vol. 7476 LNCS, 2012, pp. 113–122, 10.1007/978-3-642-32717-9-12.

[19] Y. Hu, L. Miyashita, Y. Watanabe, and M. Ishikawa, "Robust 6-DOF motion sensing for an arbitrary rigid body by multi-view laser Doppler measurements," *Optics Express*, Vol. 25, No. 24, 2017, 10.1364/oe.25.030371.

[20] H. Schaub and J. L. Junkins, *Analytical Mechanics of Space Systems*. Reston, VA: AIAA Education Series, 3rd ed., 2014, 10.2514/4.102400.

[21] D. W. Adams, M. Majji, S. Urdahl, T. Kulkarni, A. Katake, A. S. Martin, and E. Skulsky, *Velocimeter LIDAR-Based Bulk Velocity Estimation for Terrain Relative Navigation Applications*, 10.2514/6.2022-2208.

[22] J. L. Crassidis and J. L. Junkins, *Optimal estimation of dynamic systems*. CRC press, 2011.

[23] R. Zanetti and K. J. DeMars, "Joseph formulation of unscented and quadrature filters with application to consider states," *Journal of Guidance, Control, and Dynamics*, Vol. 36, No. 6, 2013, pp. 1860–1863, 10.2514/1.59935.

[24] F. M. Ham, "Determination of the degree of observability in linear control systems," *Retrospective Theses and Dissertations*, 1980, p. 6727.